ADVANCING EARTH AND SPACE SCIENCES

JGR Solid Earth

RESEARCH ARTICLE

10.1029/2026JB033912

Geometric Moment Modulated and Maximum Entropy Informed Earthquake + Afterslip Sequences

Brendan Meade[1]

[1]Department of Earth & Planetary Sciences, Harvard University, Cambridge, MA, USA

Key Points:

- Earthquake sequences are generated without requiring knowledge of stress or friction
- An uncertainty maximizing approach is used to determine earthquake locations
- Ensembles of synthetic loading-dependent, finite-slip, earthquake sequences can be generated cheaply

Correspondence to:

B. Meade,
meade@fas.harvard.edu

Citation:

Meade, B. (2026). Geometric moment modulated and maximum entropy informed earthquake + afterslip sequences. *Journal of Geophysical Research: Solid Earth*, *131*, e2026JB033912. https://doi.org/10.1029/2026JB033912

Received 26 JAN 2026
Accepted 17 AUG 2026

Author Contributions:

Conceptualization: Brendan Meade
Formal analysis: Brendan Meade
Investigation: Brendan Meade
Methodology: Brendan Meade
Software: Brendan Meade
Validation: Brendan Meade
Visualization: Brendan Meade
Writing – original draft: Brendan Meade
Writing – review & editing: Brendan Meade

Abstract Synthetic earthquake sequences may be of interest for comparisons with seismicity and afterslip evolution from instrumental observations and deeper time paleoseismic event histories, as well as for forecasting purposes. Here, we describe a constructed method, independent of continuum mechanics, for generating long-duration earthquake and afterslip sequences relying on an approximate geometric moment balance approach for earthquake rates and maximum entropy approaches for both earthquake centroid probabilities and afterslip speeds. Earthquake rates are proportional to geometric moment deficit and an additive Omori style aftershock term. Coseismic event centroid likelihoods are modeled as dependent on the spatial distribution of geometric moment and event magnitudes. We show how this model can be used to generate ensembles of earthquake sequences and to calculate the sensitivity of coseismic event evolution to differences in spatial patterns of geometric moment accumulation.

Plain Language Summary We describe a method for generating long earthquake and afterslip sequences, with a focus on kinematics and on maximizing uncertainty rather than on rock mechanics. This method is based on an approximate balance between tectonic motions and fault slip. Earthquake locations are determined using an uncertainty maximizing approach approach that favors minimal commitment unless additional guiding information is available. Small earthquakes can happen almost anywhere, while large earthquakes are more likely to occur where more slip has accumulated. Post-earthquake afterslip is included and tuned to contribute approximately 10%–20% of the slip release budget. By comparing multiple simulations, we show how earthquake sequences can vary due to randomness and changes in the location of fault loading.

1. Introduction

Observations of earthquake sequences may be approximately split into two categories: (a) sequences from instrumental (seismic, geodetic, gravitational) measurements and (b) sequences from paleoseismic/geologic investigations. Regional seismic sequences from the first category may include millions of events (for example, Ross et al., 2019; Yano et al., 2017) are generally limited to a few decades (i.e., the duration of dense instrumentation). In contrast, paleoseismic catalogs may stretch back thousands of years (for example, Fan et al., 2025; Lu et al., 2020; Weldon et al., 2002) but are largely considered to sample mostly large events (e.g., $M > 6$) and provide information only at specific geologic locales. The relative paucity of long-time-series earthquake sequence records (e.g., repeated large events, aftershocks, background seismicity, and quiescent periods) has provided at least one motivation for developing models to generate synthetic earthquake sequences. Additional motivations for developing earthquake sequence models may include applications to seismicity forecasting and efforts to connect seismicity with ideas in, but not limited to, statistics (Ogata, 1988) and dynamical systems (Herz & Hopfield, 1995).

A range of earthquake sequence models have been developed, and these might be categorized as (a) mechanics-focused, (b) statistical/machine learning, and (c) constructed/heuristic. Mechanics-focused models consider the time-dependent behavior of fault slip rates in response to evolving stresses, material properties, and fluid-modulated rate-and-state friction laws. Theoretical and computational studies have demonstrated how these mechanical concepts can give rise to fast (coseismic) (for example, Dunham, 2007; Lapusta & Rice, 2003; Lapusta et al., 2000; Rice & Tse, 1986; Rice et al., 2001; Shaw, 1995) and slow slip (for example, Barbot et al., 2009; Johnson et al., 2006; Liu & Rice, 2005; Rubin, 2008; Savage & Langbein, 2008), as well as explain a variety of both specific faulting observations (for example, Biemiller et al., 2023; Kaneko et al., 2010; Kozdon & Dunham, 2013; Lambert et al., 2021; Wei et al., 2013). Mechanical models of earthquake sequences also provide a means of connecting microscopic fault state representations (e.g., stress, friction) and properties to macroscopic behaviors, including rupture extent and timing (for example, Burridge & Knopoff, 1967; Erickson et al., 2020, 2023; Kaneko et al., 2010; Rice & Tse, 1986; Richards-Dinger & Dieterich, 2012; Rundle et al., 2006). Statistically focused earthquake sequence models provide a means of generating earthquake sequences that may be independent of, or only weakly linked to, mechanical ideas regarding fault slip. For example, aftershock triggering has been described in terms of point processes (for example, Ogata, 1988; Ogata & Zhuang, 2006), purely statistical (for example, Terada, 1933], and the potential predictability of classes of $M < 5$ earthquakes has been represented with machine learning approaches (for example, Dascher-Cousineau et al., 2023; Zhang et al., 2024) and the possibility of more predictable large events in a dynamical systems setting (Venegas-Aravena & Zaccagnino, 2025). In each of these cases, models use theoretically motivated, assumed, or learned transfer functions to relate a set of observables to future seismicity rates, with applications primarily to relatively short-term (weeks to years) earthquake sequences. In contrast, constructed and heuristic models have been developed with a focus extending to longer time scales (years to millennia). These include ideas based on the tracking of strain budgets (for example, Neely et al., 2023; Salditch et al., 2020). Note that there aren't necessarily sharp boundaries between model classifications, as, for example, spring-slider models have been augmented with rate-and-state friction (Filippov & Popov, 2010; Rice & Tse, 1986) and point process models have been adapted to include stress transfer ideas (for example, Asayesh et al., 2025; Borovkov & Bebbington, 2003).

Non-mechanical models of earthquake sequences may be motivated by the idea that there may be representations of earthquake sequence behaviors that do not require knowledge of the microscopic state of a system nor the problem-solving framework of continuum mechanics. Attempts at macroscale earthquake sequence models include, but are not limited to, neuron-like triggering (Herz & Hopfield, 1995), kinematic block-and-fault (for example, Ismail-Zadeh et al., 2007; Ismail-Zadeh & Soloviev, 2022), heuristic-focused (Meade, 2024), and strain tracking (Salditch et al., 2020; Neely et al., 2023) models. Outside of earthquake science, a more general perspective is foundational in thermodynamics, with Carnot (1824) stating, “In order to consider in the most general way the principle of the production of motion by heat, it must be considered independently of any mechanism or any particular agent. It is necessary to establish principles applicable not only to steam engines but to all imaginable heat engines” (Thurston, 1897). The core idea being that microscopic processes and states may be difficult to measure at the required scale, chaotic, too numerous to meaningfully represent, or that there may not be a uniquely knowable model of mechanical behavior. Here, we develop an explicitly macroscopic approach for earthquake sequence generation that depends on a suite of statistical relationships linked by the idea that, in the absence of other information, we might consider maximizing uncertainty using maximum entropy methods (Jaynes, 1957b, 1957a).

2. A Kinematically Modulated and Maximum Entropy Informed Earthquake Sequence Generator

We develop an earthquake sequence simulator predicated on the integration of approximate moment balance, observed macroscopic scalings, maximum entropy formalism, and arbitrary choices. There are three core parts. The first is a moment budget (for example, Bilham & Ambraseys, 2005; Jackson, 1996) modulated earthquake rate calculation. This component is kinematically focused, forces models toward geometric moment, m, conservation (where moment release from fault slip is approximately balanced by tectonic moment accumulation in the absence of fault slip), and does not rely, at least not directly, on maximum entropy ideas. Geometric moment is defined as the product of the area of some section of a fault and average slip on that same section (for example, Ben-Zion, 2001). The second and third components of the constructed earthquake sequence generator are formulations for coseismic event locations and afterslip rates, both of which use maximum entropy approaches (for example, Jaynes, 1957b; Thurner et al., 2018).

2.1. A Geometric Moment Budget Dependent Formulation for Earthquake Rates

The total number of earthquakes up to time t is $n(t) = \int_0^t \rho(t')\,dt'$, where ρ is the rate of earthquake occurrence. In this formulation, the rate of earthquakes accumulates so that $n(t)$ may be greater than one even if $\rho(t)$ is less than one at a particular time. The earthquake rate is assumed to have the form,

$$\rho(t) = c\,\dot{m}_{\mathrm{d}}(t) + \rho_{\mathrm{o}}(t) \tag{1}$$

where c is a constant determined to promote geometric moment deficit, balance, or excess, m_d is the geometric moment deficit, and ρ_o is an Omori style accelerated rate of event occurrence following earthquakes and quantized as a function of event magnitude M (Reasenberg & Jones, 1989). The geometric moment deficit is defined as the difference between geometric moment accumulation rate, $\dot{m}_\mathrm{a}$, and geometric moment release by both coseismic, m_c, and slow slip activities, $\dot{m}_\mathrm{s}$ (e.g., afterslip, slow slip events),

$$\dot{m}_\mathrm{d}(t) = \int_0^t \dot{m}_\mathrm{a}(t')\,dt' - \left[\sum_{i=0}^{n(t)} m_\mathrm{c}^i + \int_0^t \dot{m}_\mathrm{s}(t')\,dt'\right]. \tag{2}$$

The inclusion of slow postseismic slip in geometric moment budget calculations may be quantitatively meaningful as afterslip following large earthquakes may characteristically release 9%–32% of the geometric moment of the mainshock (Churchill et al., 2022).

A value for c can be derived if we assume an approximate long-term geometric moment balance. We do this by representing the average earthquake rate, $\bar{\rho}$, in two ways. First, one statement of geometric moment balance at equilibrium can be, $\dot{m}_\mathrm{r} = \bar{\rho}\bar{m}$ where $\bar{m}$ is an average moment over all of earthquakes, which can be determined from the weighted average of the geometric moment release rates drawn from a Gutenberg-Richter distribution, $\bar{m} = \int_{M_\mathrm{min}}^{M_\mathrm{max}} m(M)N(M)dM$. Here M_min and M_max are prescribed minimum and maximum event magnitudes, $m(M)$ is the moment magnitude to moment relationship, and $n(M)$ is the probability of an event magnitude drawn from the Gutenberg-Richter distribution. Note that arguments have been previously advanced (Berrill & Davis, 1980; Page & Field, 2026) suggesting ways in which Gutenberg-Richter like relationship itself may emerge from entropy oriented arguments for an idealized single fault geometry case, and that we assume the relationship holds generally and informs. A second relationship for the average rate of earthquake occurrence, neglecting transient Omori effects, is $\bar{\rho} = cm^*$ where m^* is a typical accumulated geometric moment at equilibrium. If we assume that the geometric moment accumulation rate is constant in time and that the geometric moment release is dominated by largest coseismic events then a characteristic time scale for the recurrence of the largest events could be, $t_\mathrm{r} = m_\mathrm{max}/\dot{m}_\mathrm{a}$, and the average accumulated geometric moment is, $m^* = \dot{m}_\mathrm{a}t_\mathrm{r}/2$. Equating these two representations of $\bar{\rho}$ gives $c = 2\dot{m}_\mathrm{a}/\bar{m}m(M_\mathrm{max})$. Note that this expression is applicable to the case of approximate geometric moment balance, and lesser and greater values of c will lead to coseismic geometric moment deficits and excesses, respectively.

If the accumulated earthquake rate exceeds one, an earthquake, or multiple earthquakes if $\rho > 2$, is generated at a time step. First, an event magnitude is selected from the Gutenberg-Richter distribution. Second, the magnitude is converged into an approximately rupture area using the empirical scaling relationship $\log_{10}(a) = M - 3.99$, where a is the rupture area in square kilometers (Allen & Hayes, 2017). This scaling relationship is an assumed heuristic that lies outside of the maximum entropy approach. A circular region is expanded around the centroid location of the earthquake (Section 2.2) until sufficient area is accumulated for a given event size. Each rupture here is assumed to be circular unless it is truncated when reaching a fault boundary. Inside of each coseismic slip region, there is an exponential decrease in slip away from the event centroid and additive perturbations drawn from a uniform distribution. All potentially slipping fault elements are checked to ensure that they have no more slip than the available geometric moment on the patch. Finally, the slip pattern is uniformly scaled to match the target geometric moment. Note that the coseismic slip patterns used here are intentionally simple and that alternative statistical representations could be applied (Mai & Beroza, 2002; LeVeque et al., 2016). After the slip generation for an earthquake (or set of earthquakes), both the global geometric moment budget (Equation 2) and earthquake production rate (Equation 1) are updated. All calculations are performed relative to a background "spun-up" geometric moment-budget state, representing the assumption that the fault has been active for a long time prior to a particular realization of model time. This ensures that there is never any negative moment, so that no fault element can slip so much that it exceeds the absolute moment deficit.

2.2. A Maximum Entropy Approach to Earthquake Location Probabilities

Before proceeding with the model development, it's worth spending a few words on nomenclature. The approach used here is based on the ideas developed in Jaynes' 1957 papers (Jaynes, 1957b, 1957a). There, the terminology "maximum entropy" is used to describe a statistical mechanics approach to developing frequency distributions that are "maximally uncertain" and "minimally committal" subject to constraints. We use the terminology maximally entropy loosely because we use both the discrete Shannon entropy and a continuous relative entropy (for example, Thurner et al., 2018), and we do not intend to connect the maximum entropy/uncertainty approach to the maximum entropy production principle (for example, Prigogine, 1978; Martyushev & Seleznev, 2006) or as applied to earthquake problems (for example, Main & Naylor, 2008, 2012; Vallianatos et al., 2016). Finally, it's also worth noting that all derived relationships here have simple power-law and exponential functional forms. All of these could be guessed at, and the approach developed here simply provides a rationale in the style of statistical mechanics.

The central idea here is to calculate earthquake centroid location probabilities in a way i.e. maximally non-commital, subject to constraints, using the maximum entropy approach that maximizes uncertainty subject to applied constraints (for example, Jaynes, 1957b, 1957a; Thurner et al., 2018). For the earthquake centroid calculation, we assume three constraints. First, the probabilities for occurrence somewhere on a fault surface of interest are normalized. $\sum_{i=1}^{N} p(i|m) = 1$ where i indicates some discretized subsection of a fault (i.e., a fault patch). Second, that expected geometric moment of coseismic events is distributed logarithmically, $\langle \log m \rangle = \sum_{i=1}^{N} p(i|m) \log m_i$. This choice is motivated by the frequent appearance of power-law and logarithmic terms in statistical seismology (for example, Ben-Zion, 2008) and because the logarithms of multiplicative rupture quantities add. Other extensive variable choices may be sensible. Third, we assume that the expected logarithmic geometric moment may depend on the event magnitude. This allows us to encode the idea that large earthquakes are more likely to occur in regions with higher accumulated geometric moment, but that smaller magnitude events are more likely to occur over regions of both high and low geometric moment accumulation (for example, Oryan & Gabriel, 2025; Venegas-Aravena & Zaccagnino, 2025).

For a discrete probability distribution, the information entropy (Jaynes, 1957b) is $S \propto -\sum_{i=1}^{N} p(i|M) \ln p(i|M)$, which is maximally non-committal with regard to earthquake location when $p_i = 1/N$ for all i. To maximize S subject to these constraints, we form the function,

$$\begin{aligned} \mathcal{L}_{\mathrm{c}} = & -\sum_{i=1}^{N} p(i|M) \ln p(i|M) \\ & -\lambda_{\mathrm{c}}^{\{1\}}(M)\left[\sum_{i=1}^{N} p(i|M) - 1\right] \\ & -\lambda_{\mathrm{c}}^{\{2\}}(M)\left[\sum_{i=1}^{N} p(i|M) \log m_i - \langle \log m \rangle_M\right] \end{aligned} \tag{3}$$

where $\lambda_{\mathrm{c}}^{\{1\}}(M)$ is the Lagrange multiplier to ensure probabilities sum to one and $\lambda_{\mathrm{c}}^{\{2\}}(M)$ is the Lagrange multiplier for the constraint that earthquakes of magnitude M, on average, are located at in regions where the log-geometric moment availability has a particular expected value, $\langle \log m \rangle_M$. To solve for $p(i|M)$, we differentiate Equation 3 and solve for the Lagrange multipliers to get a canonical maximum entropy distribution,

$$p(i|M) = \frac{m_i^{\lambda_{\mathrm{c}}^{\{2\}}(M)}}{\sum_j m_j^{\lambda_{\mathrm{c}}^{\{2\}}(M)}}. \tag{4}$$

The expectation of logarithm distribution of coseismic geometric moments can be used to form an implicit equation for $\lambda_{\mathrm{c}}^{\{2\}}$,

$$\sum_{i=1}^{N} \frac{m_i^{\lambda_{\mathrm{c}}^{\{2\}}(M)}}{\sum_j m_j^{\lambda_{\mathrm{c}}^{\{2\}}(M)}} \log m_i = \langle \log m \rangle_M. \tag{5}$$

To solve for $\lambda_{\mathrm{c}}^{\{2\}}(M)$ we assume a smooth distribution of geometric moment values and expand in series keeping only the first non-constant term, $\langle \log m \rangle \approx a + b\lambda_{\mathrm{c}}^{\{2\}}$ to get the approximation $\lambda(M) \approx \left(\langle \log m \rangle_M - a\right)/b$.

Substituting the magnitude-dependent constraint $\langle \log m \rangle_M = \langle \log m \rangle_{\max} - \Delta g e^{-\alpha(M - M_{\min})}$, into the linear approximation gives,

$$\lambda_{\mathrm{c}}^{\{2\}}(M) = \lambda_{\max} - (\lambda_{\max} - \lambda_{\min})\, e^{-\alpha(M - M_{\min})}. \tag{6}$$

At minimum magnitude, $\lambda_{\mathrm{c}}^{\{2\}}(M_{\min}) = \lambda_{\max} - (\lambda_{\max} - \lambda_{\min}) = \lambda_{\min}$ so that small events have low selectivity for accumulated geometric moment deficit while large magnitude λ values have high selectivity prompt the preferential occurrence of large magnitude events in regions of relatively high accumulated geometric moment. We define $\lambda_{\min} = 0$ so that the locations of the smallest earthquakes are independent of accumulated geometric moment. By fiat, we define $\lambda_{\max} = 1$ and $\alpha = 1$ so that larger events are more likely to occur in regions of high accumulated geometric moment. Alternatively, there may be principled or empirical approaches to representing $\lambda_{\min}$, $\lambda_{\max}$, and α.

2.3. A Maximum Entropy Approach to Time-Dependent Afterslip

We seek a description of postseismic afterslip rates v that varies in time and is relatively spatially localized near to, and possibly coincident with, the area of coseismic rupture, assuming that the spatial and temporal terms are separable, $v(r_i, t) = \phi(r_i)\sigma(t)$.

Following a coseismic event, a fault patch may have a positive residual geometric moment, m_i^{r}. Afterslip may occur in these regions, further decreasing previously stored geometric moment, $\dot{m}_i^{\mathrm{r}} = -\sigma_i a_i$. Again using the maximum entropy distribution, we seek a probability distribution for afterslip speeds, $p(\sigma_i)$, that is minimally committal. For a continuous afterslip speed σ, we maximize the relative entropy (Jaynes, 1957b), $S = -\int_0^\infty p(\sigma_i) \log(p(\sigma_i)/m(\sigma_i))\, d\sigma_i$, subject to constraints encoding what we know about the system. Here, $m(i)$ is a measure of how afterslip velocities would be distributed in the absence of any constraints, and we assume that it is a constant, consistent with a minimally committal philosophy. The constraints are that the probabilities sum to one, $\int_0^\infty p(\sigma_i)\, d\sigma_i = 1$, and that there is a finite expected velocity with an unknown value that we will prescribe or solve for, $\int_0^\infty \sigma_i p(\sigma_i)\, d\sigma_i = \bar{\sigma}$. As before, we use Lagrange multipliers and maximize,

$$\mathcal{L}_{\mathrm{a}} = -\int_0^\infty p(\sigma_i) \log p(\sigma_i) - \lambda_{\mathrm{a}}^{\{1\}}(\sigma_i)\left[\int_0^\infty p(\sigma_i) - 1\right] - \lambda_{\mathrm{a}}^{\{2\}}(\sigma_i)\left[\int_0^\infty \sigma_i p(\sigma_i) - \overline{\sigma_i}\right]. \tag{7}$$

Solving for the partition function gives the normalized probability of an afterslip velocity, $p(\sigma_i) = e^{-\sigma_i \lambda_{\mathrm{a}}^{\{2\}}} / \int_0^\infty e^{-\sigma \lambda_{\mathrm{a}}^{\{2\}}} d\sigma$. The quantity $\lambda_{\mathrm{a}}^{\{2\}}$ controls how readily a patch slips, with large and small values associated with slip distributions concentrated near zero and broad distributions extending to high velocities, respectively. We propose that the driving potential for afterslip is the residual geometric moment, m_i^r, so that a patch with a large residual geometric moment has more capacity to slip than one with a small residual geometric moment. We also propose that the potential for afterslip is linearly proportional to the residual geometric moment, so that the afterslip speed evolves as $\sigma_i(t) = \kappa^{-1} m_i^{\mathrm{r}} e^{-t a_i/\kappa}$ with the single parameter κ controlling both the afterslip timescale and initial velocity magnitude.

We assume that the spatial distribution of afterslip is controlled by three key components that multiply together to determine the evolution of slip velocity, $v_i(t = 0) = \sigma_{\mathrm{scale}}(m, t)\phi(r_i)\, m_{\mathrm{r},i}$, where σ_{scale} is a magnitude-dependent velocity scale, $\phi(r_i)$ is a spatial activation kernel, and $m_{\mathrm{r},i}$ is the residual geometric moment deficit at each patch. The kernel $\phi(r_i)$ controls where afterslip can occur and is assumed to be exponential, $\phi(r_i) = e^{-r_i/l}$, and we use the same spatial kernel for an enhanced likelihood zone for aftershocks. Note that alternative afterslip distance decay functions could be displacement/moment, r^{-2}, stress, r^{-3}, or strain energy change, r^{-6}, but here we are working to develop an approach that is detached from any particular continuum mechanics statements. Also note that here we assume afterslip might occur on patches that rupture coseismically (Johnson et al., 2012; Meade, 2024) but that one could construct spatial kernels that preclude this. The velocity scale factor is assumed to have the form $\sigma_{\mathrm{scale}} = \sigma_0 (M/M_{\mathrm{ref}})^\beta$, where is assumed to be $\sigma_0 = 0.1$ m/yr for $M_{\mathrm{ref}} = 7.0$. We assume $\beta = 1/3$, motivated by the idea that geometric moment scales as the cube of a characteristic length scale, and note that this may not be an appropriate assumption for earthquakes ruptures that are ribbon-like and deviate from circular-like shape. This dependence on residual geometric moment means that afterslip may, but does not necessarily, occur both inside

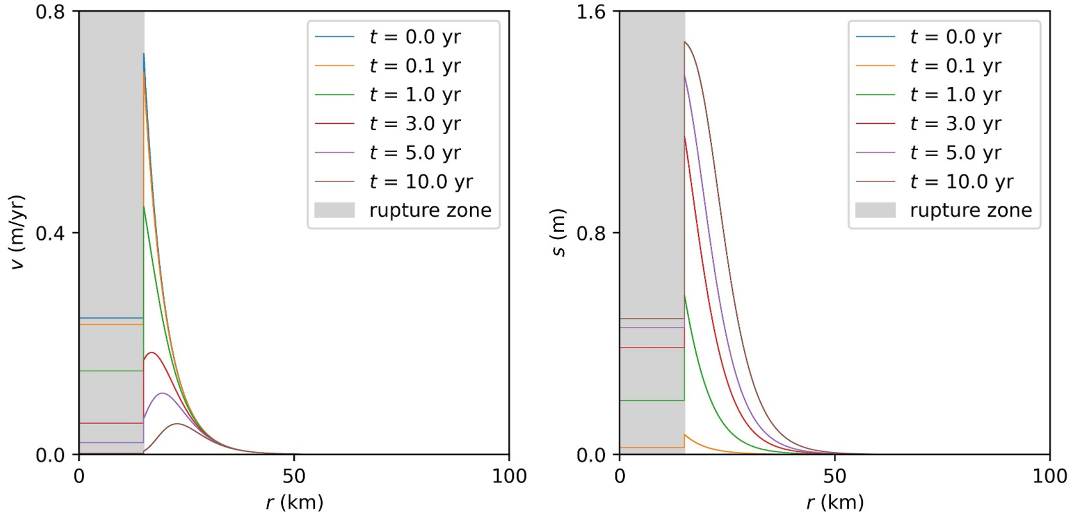

Figure 1. Radial profiles of afterslip velocity (left) and cumulative afterslip (right) as a function of distance from the rupture center at six time snapshots ($t = 0.0$, 0.1, 1.0, 3.0, 5.0, and 10.0 years). The gray shaded region indicates the coseismic rupture zone ($r < 15$ km). In this particular case, the coseismic slip did not reduce the accumulated geometric moment in the rupture to zero, so some afterslip occurs in the coseismic rupture area but reaches a maximum value in a halo surrounding the rupture area, where geometric moment deficits and proximity to the coseismic rupture are both large. Afterslip velocities reach a maximum at the rupture edge ($r \approx 15$ km), where the spatial activation kernel and accumulated geometric moment are both large, then decay with increasing distance. Cumulative slip accumulates preferentially in the near-field halo, with the radial distribution broadening over time as afterslip propagates outward.

and outside of a region that slips coseismically. Inside the coseismic rupture area, ϕ may approach one, but whether or not afterslip occurs in this region depends on the sign of the residual geometric moment left after the earthquake (Figure 1). Adjacent to the coseismic rupture area, ϕ is still relatively large, and coseismic slip will not have released geometric moment here, so afterslip may reach a maximum here before decaying with distance (for example, Churchill et al., 2022). Combining this definition of $\phi(r_i)$ and the per-patch afterslip speed evolution, $\sigma(t)$, we find,

$$v(r_i, t) = \frac{m_i^{\mathrm{r}}}{\kappa e^{t a_i/\kappa + r_i/l}}. \tag{8}$$

2.4. An Example Earthquake + Afterslip Sequence Realization

As an example of the application of the earthquake + afterslip generation Algorithm (see 1) we generate a 1,000 years long earthquake and afterslip sequence on a synthetic (200 km long by 25 deep, discretized into 0.5×0.5 km elements) vertical strike-slip fault with a single slip component. The fault is loaded at a background rate of 10 mm/yr across all elements, augmented by a single Gaussian geometric moment-rate pulse (20 mm/yr amplitude, 25 km length scale) centered at $x = 100$ km as a source of spatial heterogeneity. Event magnitudes drawn from a Gutenberg-Richter distribution with $b = 1.0$ over the range $M = 5.0\text{–}8.0$ and the magnitude sensitivity to accumulated geometric moment is modulated by $\gamma_{\min} = 0$ so that small events may nucleate anywhere and $\gamma_{\max} = 1.5$ so that large events are more likely to be centered where where accumulated geometric moment is relatively high. Enhanced event likelihoods follow all events with an Omori-like rate increase (Equation 1), a decay time of one day, and magnitude-dependent productivity (Reasenberg & Jones, 1989), tracked for 30 years after each mainshock. Note that synthetic earthquake catalogs calculated with this method recover the prescribed Gutenberg-Richter b value (because nothing modulates the event size) but do not generate aftershock sequences with Omori exponent values identical to those prescribed. The reason for this is the interplay between the Omori aftershock rate calculation and the evolving moment deficit, which can include both short-term suppression of event rates and increases over longer periods as the loading effect becomes prominent. In the examples below, the prescribed Omori exponent is 1, and values calculated from synthetic catalogs are 0.55–0.75. Note that while we do not provide any prior assumptions about the existence of Bath's law-like behavior, these simulations produce $\Delta \mathrm{M_W} = 0.61\text{–}0.87$, indicating maximum aftershock sizes that are larger

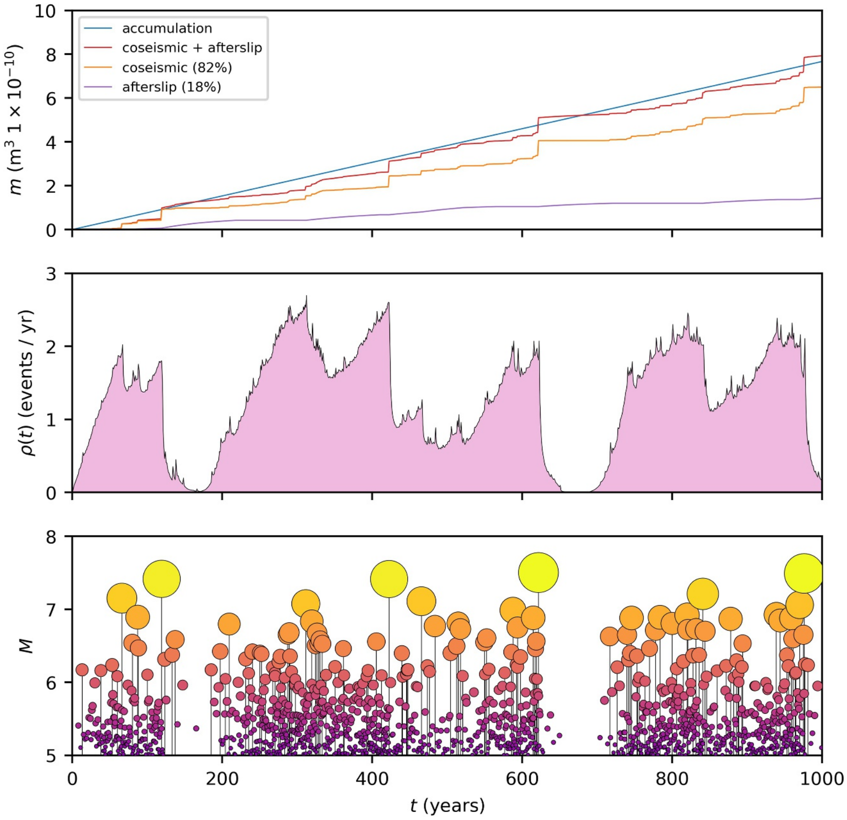

Figure 2. Time evolution of geometric moment budget, seismicity rate, and earthquake magnitudes for a single 1000 years long realization. Upper panel: Cumulative geometric moment showing prescribed steady tectonic accumulation (blue) approximately balanced by total geometric moment release (red), partitioned into coseismic slip (orange, 82%) and aseismic afterslip (purple, 18%). Middle panel: Instantaneous earthquake rate $\rho(t)$. The rate increases steadily in the absence of earthquakes and afterslip, dropping with the occurrence of large events that release geometric moment both coseismically and through triggered afterslip. Bottom panel: Coseismic event magnitude time series with symbol size and color scaled by magnitude. Event clustering corresponds to high-rate periods in the middle panel, while quiescent intervals (e.g., $t \sim 150$–200, $600-700$ years) follow some, but not all, large earthquakes. Note that in this particular example aftershock productivity is prescribed to be relatively low simply to produce visually clear, albeit more idealized large earthquake time series.

than the empirical $\Delta M_W = 1.1-1.2$ (Båth, 1965). Also, following $M \geq 7.0$ events, with initial velocity 0.01 m/yr at $M = 7.0$, spatial extent determined by an exponential spatial decay kernel with 10 km length scale, active for 100 years per sequence. Afterslip is tracked for 100 years, 70 years longer than aftershocks, because the former is assumed to release greater moment.

Over 1,000 simulated years, the perturbed geometric moment accumulation rate is 97% of the geometric moment release, with afterslip accounting for 18% of the geometric moment release budget. The realization generated 1,272 earthquakes, including 849 events in the $M = 5.0$–5.5 range and 9 $M \geq 7.0$ events, the largest being a $M = 7.5$ event, occurring at $t = 621$ years. Event centroids span the full fault but show preferential nucleation near the Gaussian loading pulse with 27% of events nucleated within 25 km of the pulse centroid at $x = 100$ km despite this region comprising only 25% of fault length. As prescribed, $M \geq 7.0$ events generate afterslip both on the coseismic slip area itself and in halos surrounding the coseismic slip region (Figures 3–6). There are two 30+ year long quiescent periods (starting near 140 and 650 years) following large events with 10+ year long aftershock sequences (Figure 2). The generation of quiescent periods is not inevitable and depends on the random seed used for each realization (e.g., middle 3 panels Figure 7 showing random seed experiments). All behaviors in this example realization are prescribed by the model's construction. There are no particular emergent behaviors, with the possible exception of the timing of quiescent periods.

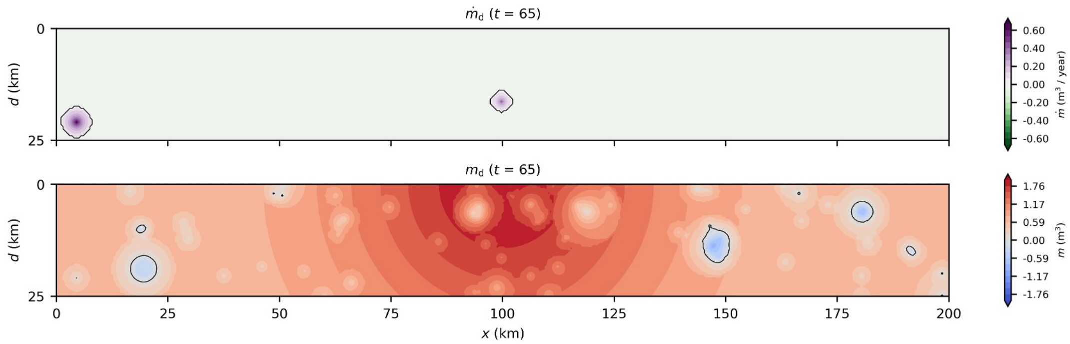

Figure 3. Snapshot of geometric moment deficit kinematics at $t = 66$ years. The upper and lower panels show the geometric moment rate, $\dot{m}_\mathrm{d}$, and cumulative geometric moment, m_d, respectively. Most of the synthetic fault is in a geometric moment deficit because no large ($M > 6.5$) earthquakes have occurred at $t = 65$ years.

3. Sensitivity to Random Seeds and Spatial Variations in Geometric Moment Accumulation

To demonstrate how the model realizations vary with different parameters, we consider two experiments, each set generating five 1,000 years long earthquake and afterslip sequences. The first set of experiments comprises model realizations that differ only in the random seed, while the second set shares a random seed but differs in the location of the Gaussian pulse that defines a region of enhanced loading. The random seed experiments generate realizations with qualitatively different behaviors in time (Figure 7) and space (Figure 8). While the central Gaussian pulse remains a preferential location for seismic events, the number of earthquakes across the five 1,000 years long model runs varies by 35% (Figure 7), and an extended duration (100+ year) quiescent epoch appears in only one model run (Figure 7 upper panel). Suites of model runs with different random seeds may have utility in the generation of ensembles of earthquake sequences used for forecasting analysis (for example, Field et al., 2017).

To develop a representation of the model's response to spatial variations in loading, we run multiple realizations where a Gaussian pulse of increased geometric moment accumulation rate is applied at different locations. In each model realization, the Gaussian pulse is shifted 1 km farther from the origin, and we track how event magnitudes and centroids differ. In these experiments, there are negligible differences in event timing because all realizations share a fixed random seed (Figure 9). Differences in event location arise purely from how the shifted probability landscape maps those draws to different mesh elements (Figure 10). In both sets of ensemble experiments the

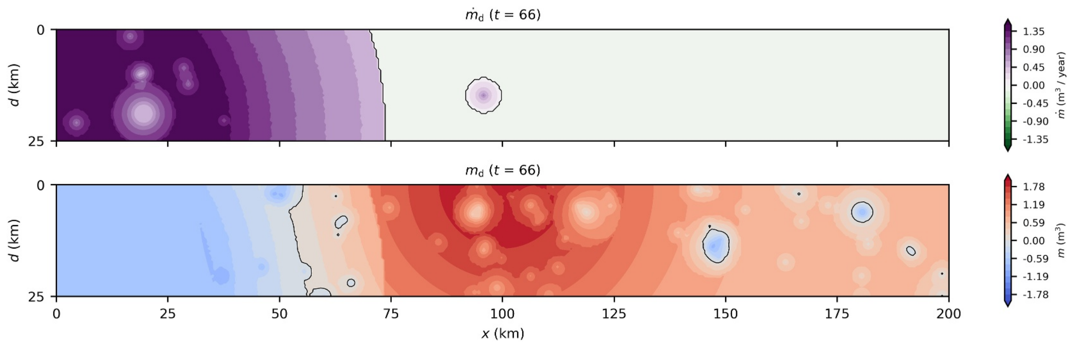

Figure 4. Snapshot of geometric moment deficit kinematics at $t = 66$ years. Upper panel: Geometric moment deficit rate, $\dot{m}_\mathrm{d}$, showing the spatial pattern of deficit accumulation and release (coseismic and afterslip). Purple regions indicate where coseismic release exceeds geometric moment accumulation. The left portion of the fault ($x < 70$ km) exhibits elevated release rates due to a $M = 7.15$ earthquake at $t = 66$ years. Aftershocks (down to $M = 5$) appear as smaller circular regions near the main shock. Lower panel: Cumulative geometric moment deficit m_d. Redish regions (positive deficit) indicate a geometric moment excess with a local concentration in a prescribed region of enhanced loading ($x \sim 75{-}125$ km). Bluish regions indicate locations where recent ruptures have released more geometric moment than has since accumulated, creating a local geometric moment deficit.

10.1029/2026JB033912

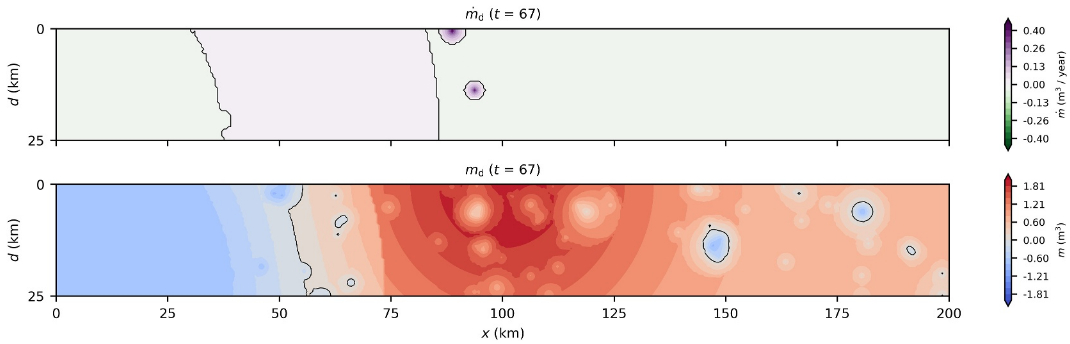

Figure 5. Same as Figures 3 and 4 but for the year after the first $M = 7.15$ earthquake. The purple band between 30 and 85 km is a region of geometric moment release due to afterslip.

recovered Gutenberg-Richter and Omori exponents (b and p respectively) are similar to the prescribed values (Figure 11) with the Omori exponent depletion caused by the addition of the post earthquake moment rate adjustment associated with large geometric moment release.

For a given magnitude and geometric moment field, the conditional entropy can be defined as $H = -\sum_i p(i|M) \log p(i|M)$, which provides a representation of the spatial uncertainty in nucleation location given the magnitude. Following the maximum entropy framework introduced previously, the effective number of elements on a mesh that might likely host an event is $N_{\text{eff}} = e^H$. We want to quantify how these changes in the assumed loading distribution give rise to transitions in the mesh cell that contains an event. To do this we define a "transition" as occurring when an event's hypocenter jumps by more than a threshold distance δ between adjacent pulse locations, $|\mathbf{x}_k(x_{\text{pulse},j+1}) - \mathbf{x}_k(x_{\text{pulse},j})| > \delta$. Because experiments with shifted loading rates indicate that larger coseismic events move slightly with changes in loading geometry (Figure 10), we can count the number of transitions for a specific event, for example, the first $M \geq 7$ event. Across an ensemble of runs the transition count, T_k (the number of indices j where the jump exceeds δ), for an event k is,

$$T_k = \text{number of } j \text{ where } |\Delta \mathbf{x}_{k,j}| > \delta \tag{9}$$

And this can be normalized by the length scale associated with the Gaussian pulse to give a type of entropy-normalized transition density measures sensitivity per unit of theoretical uncertainty $\eta = T_k / lH$. Similarly, there is a maximum value, $\eta_{\max}$, where $T_k = 1$ because there cannot be more transitions than pulse steps (Figure 12). Model realizations where $\eta \approx 1$ indicate that seismicity is being distributed maximally subject to kinematic constraints. For an extended suite of shifted Gaussian pulse experiments (shifting the pulse +1 km for 25 model realizations, Figure 10), we find that coseismic geometric moment tracks with loading (as prescribed, $R^2 \approx 0.98$) but that there is significant sensitivity to the exact location of and earthquake within regions of similar accumulated geometric moment. Note that for smaller magnitude events ($M < 6$), η values significantly

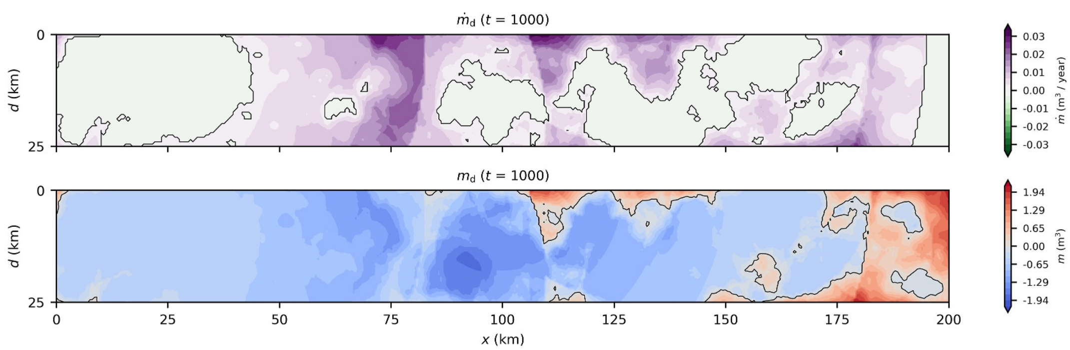

Figure 6. Same as Figures 3–5 but for the year $t = 999$. The history of past earthquakes has evolved a spatially heterogeneous distribution of geometric moment accumulation and release where the edges of some large ruptures are still discernible near $x = 80$, 110, and 185 km.

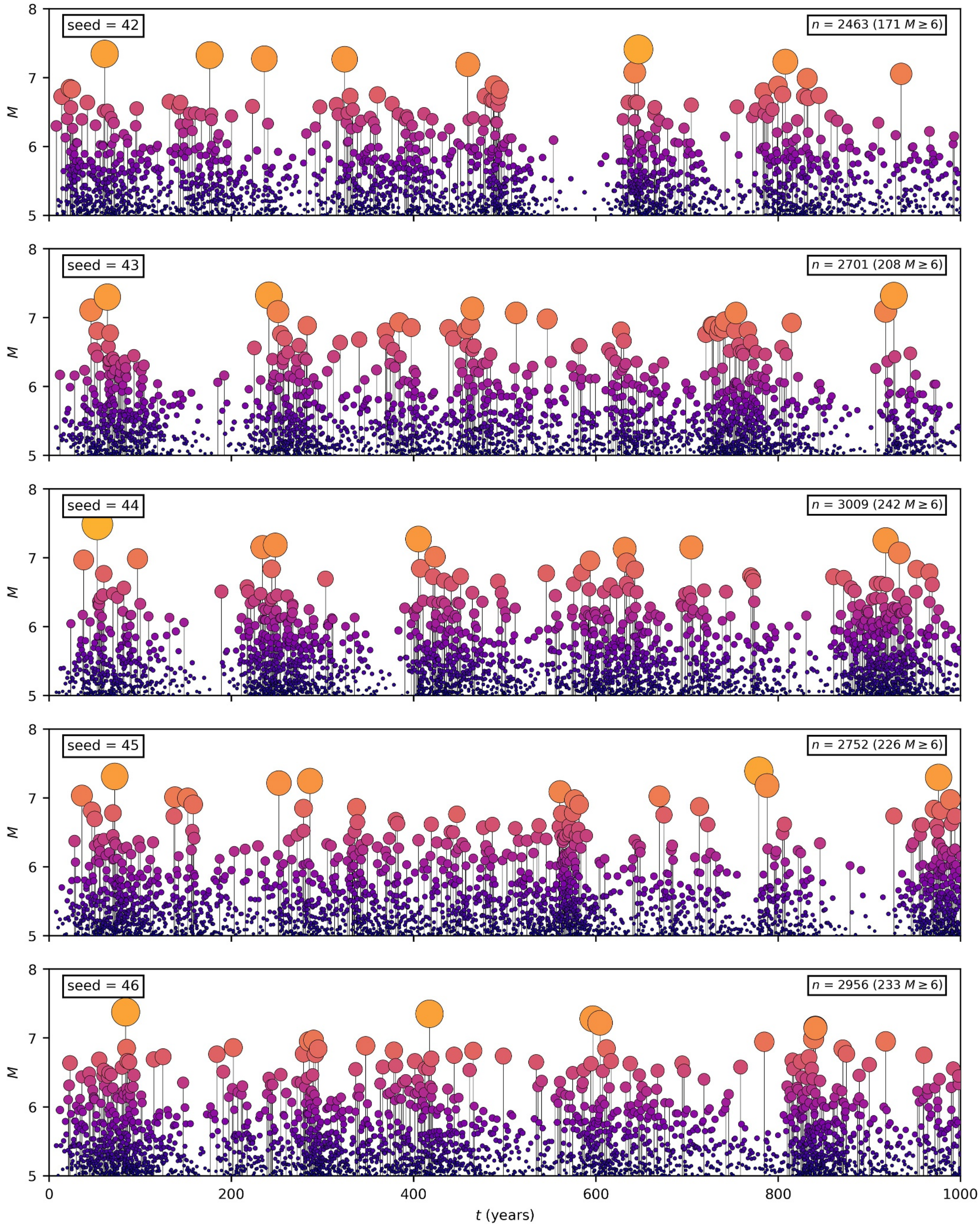

Figure 7. Magnitude-time series for ensemble simulations with varying random seeds. Each panel shows the earthquake sequence over 1000 years for seeds 42 through 46 (top to bottom), with fixed pulse location $x = 100$ km. Symbol size and color scale with magnitude. Unlike the pulse-location ensemble (previous figure), which showed identical sequences, varying the random seed produces entirely different realizations: event times, magnitudes, and total counts ($n = 376-577$) differ in their qualitative nature across realizations. The timing and number of $M \geq 7$ events varies from 3 to 6 over the 1000 years window, and quiescent periods appear at different times in each realization.

less than $\eta_{\max}$ likely indicate failures of the event tracking approach (due to the fact that smaller events are not prescribed to track positive geometric moment regions as strongly as larger events, rather than to imply the existence of some basin of attraction. These η calculations provide a sort of summary statistical representation that shows how the model may be considered close to equilibrium yet still exhibit strong sensitivity to small-scale probability variations.

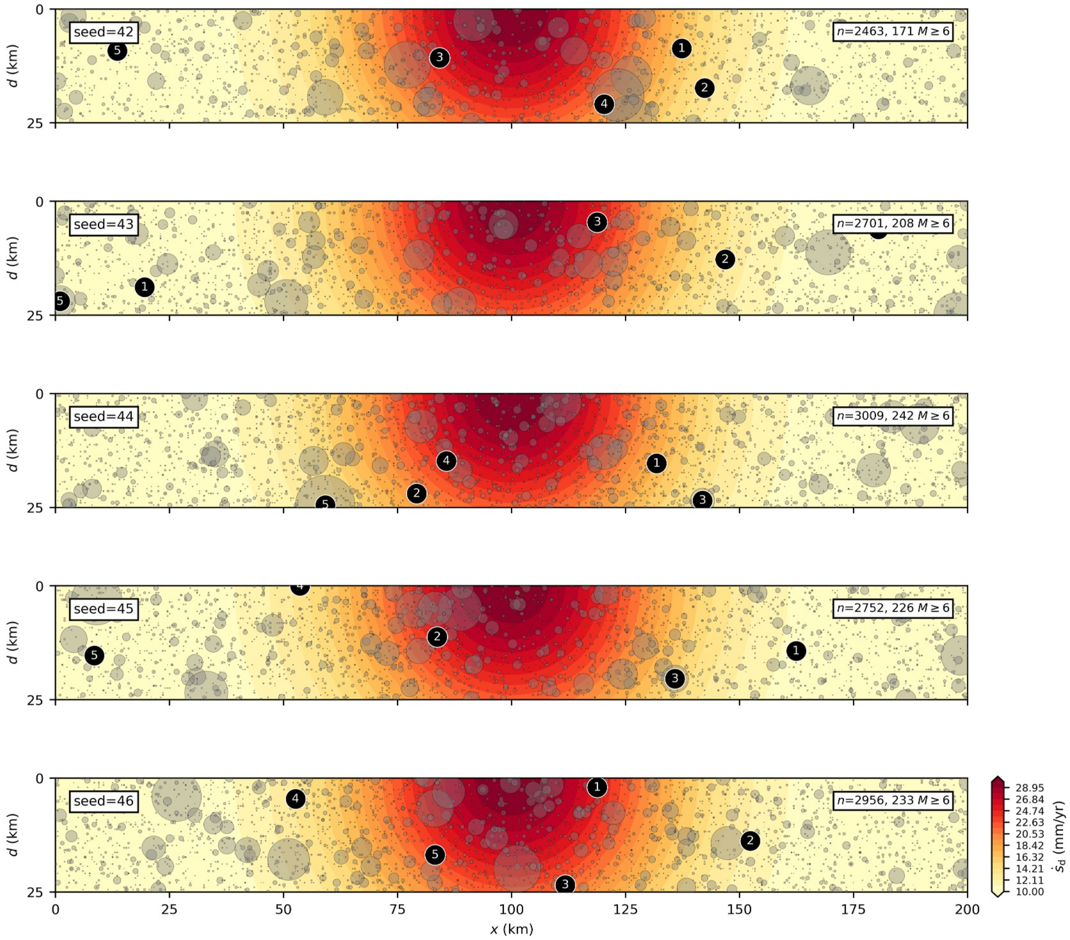

Figure 8. Example sensitivity of earthquake nucleation locations to random seed variations. Each panel shows an idealized fault plane (200 km along-strike, 25 km depth) for a simulation with a Gaussian pulse centered at $x = 100$. The number of events in these five realizations ranges from 2,463 to 3,009 over a span of 1,000 years. The contours indicate the slip-deficit (or loading) rate distribution with a localized Gaussian loading perturbation. Gray circles mark earthquake centroids with size scaled by magnitude.

4. Conclusions

For each class of earthquake sequence model, the goals are the same: Given some set of parameters, produce a series of coseismic events in time, including their locations and magnitudes (and potentially slip distributions, afterslip rates, etc.). These sequences may be intended for comparison with deep-time records (for example, Liu et al., 2022), for attempts at event forecasting, or in the interest of understanding the range of possible model behaviors. The specific earthquake sequence models we have constructed here are based on approximate moment balance, observed macroscopic scalings, maximum entropy formalism, and arbitrary choices. The model described here is build on the concept of geometric moment tracking coupled with uncertainty representations from statistical mechanics and introduces empirically motivated parameters (e.g., $\gamma_{\min}$, $\gamma_{\max}$) that might be estimated from observations in ways similar to empirical relationships for event frequency (Gutenberg & Richter, 1944), event magnitude-fault area (Allen & Hayes, 2017), and aftershock production rate (Reasenberg & Jones, 1989).

The model here shares statistical and empirical foundations with the ETAS model (for example, Ogata, 1988; Ogata & Zhuang, 2006). Philosophically, both approaches rely on either knowing or estimating parameters in statistical models, and the specific aftershock rate calculation is identical between ETAS and the model described here. With a similar conceptual foundation, numerous structural and behavioral differences differentiate the two models. One distinction is in the representation of what initiates earthquake occurrence. The classical ETAS

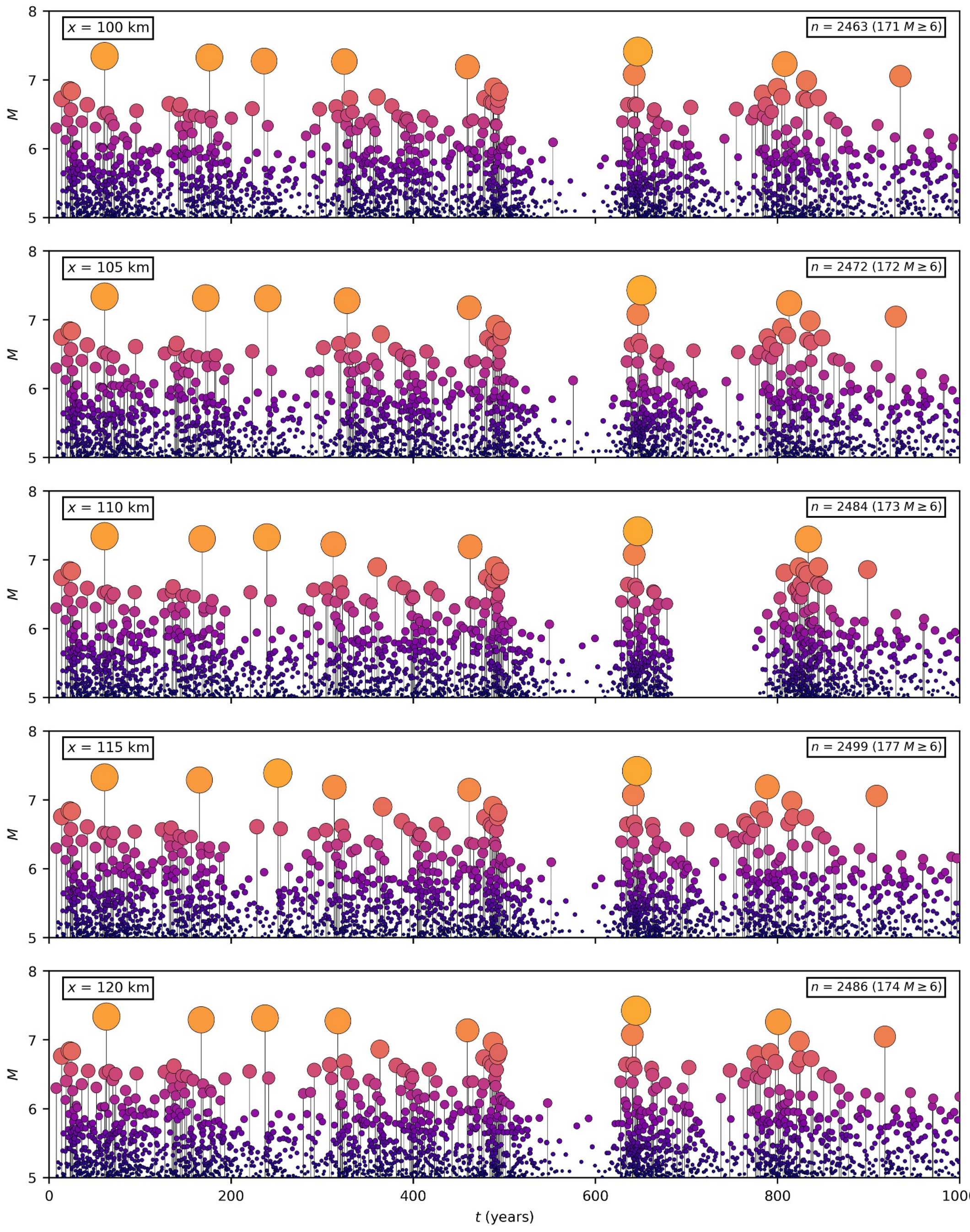

Figure 9. Coseismic event magnitude time series for realizations with simulations with varying loading pulse locations. Each panel shows the sequence of earthquakes over 1000 years for pulse center positions $x = 100$, 105, 110, 115, and 120 km (top to bottom). Symbol size and color scale with magnitude, from $M \approx 5$ (small, blue) to $M > 7.5$ (large, yellow). Vertical stems highlight events with $M \geq 6$. All simulations use identical random seeds, differing only in pulse location. The number of events varies by <1%.

approach assumes a self-exciting point process with a conditional intensity on the locations and magnitudes of past events, with no notion of stress, moment, or loading. In contrast, the model described here tracks a geometric moment field that accumulates from tectonic loading and is depleted by coseismic ruptures and afterslip, with the dominant temporal rate governed by perturbations to long term moment balance. A further difference is that the model described here represents earthquakes as spatially extended ruptures on a discretized fault, whereas classic ETAS treats events as point sources. The effects of finite area coseismic slip distribution propagate into the

10.1029/2026JB033912

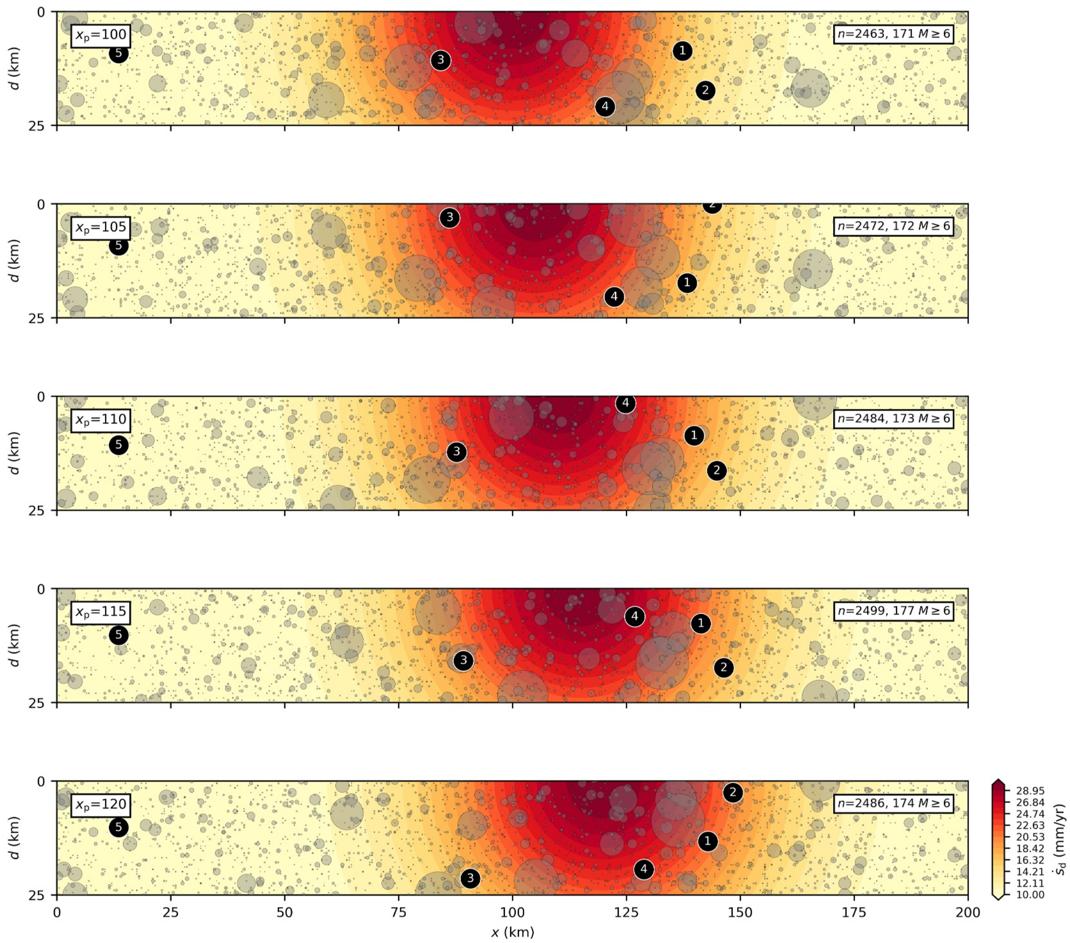

Figure 10. Sensitivity of earthquake nucleation locations to slip deficit pulse position. Each panel shows an idealized fault plane (200 km along-strike, 25 km depth) for a simulation with the pulse center shifted from 100 km (top) to 120 km (bottom) in 5 km increments. The contours indicate the slip-deficit (or loading) rate distribution with a localized Gaussian loading perturbation. Gray circles mark earthquake centroids with size scaled by magnitude. The numbered circles identify the first four $M \geq 7$ events in each realization. All realizations use identical random seeds. Events 1, 2, and 4 nucleate within the high-deficit zone and track the pulse as it shifts rightward, while the third event (located near $x \approx 30$ km) migrates upward.

maximum entropy event nucleation prior and the post-event afterslip and aftershock activation kernels. A practical consequence is that the model described in this paper produces magnitude-dependent rupture sizes and potential decreases in earthquake rates in regions where large events have recently occurred. A second spatial distinction is in how event locations are determined. ETAS models place seismic events via empirical kernels around past epicenters. The model developed in this paper selects event centroids conditioned on the current accumulated-moment field, with a prescribed magnitude-dependent selectivity so that large events preferentially nucleate where geometric moment is relatively high. The model developed here also includes a representation of afterslip, which effectively decreases the probability of local earthquakes and has no direct analog in ETAS models. Both the model described here and the ETAS model assume a memory of past earthquakes through the use of the Omori aftershock rate law. The model in this paper further adds spatial memory of where past earthquakes occurred by modulating the geometric moment state (and therefore location probabilities of future events) on the fault surface. This geometric moment loading aspect, foundational to the method described here, gives rise to behaviors including periodicity, semi-clustered large events, and quiescent epochs not exhibited by classical ETAS models, which differ from the constant background rate models. Event-time generation ETAS models are built on the assumption of a frequency distribution for event times combined with a thinning realization of the conditional intensity while the model described here relies on a deterministic rate accumulation

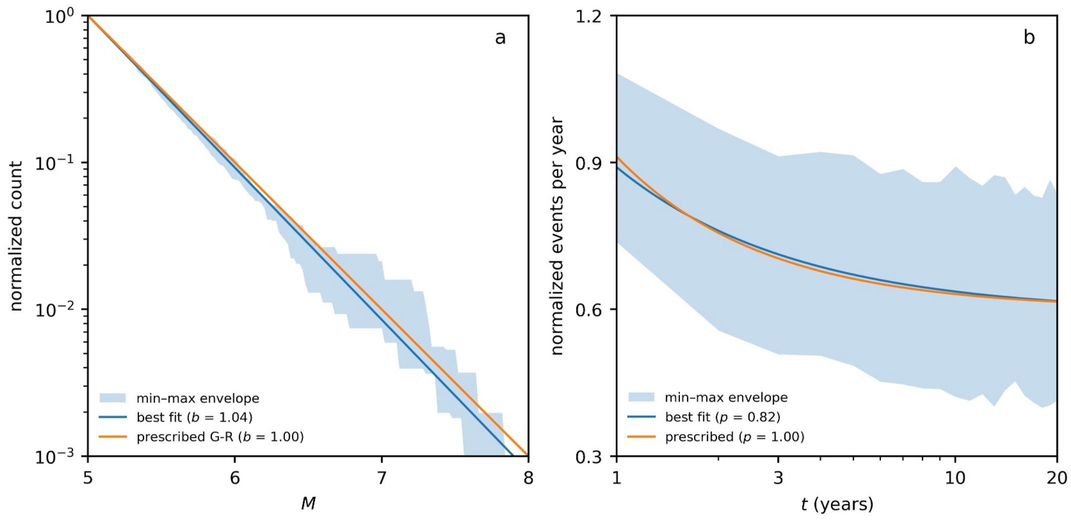

Figure 11. Prescribed and recovered earthquake statistics from ensemble simulations. Left hand panel (a): Normalized cumulative prescribed (orange line, $b = 1.00$) and recovered (blue line, $b = 1.04$) Gutenberg-Richter style magnitude distribution. Right hand panel (b): Normalized prescribed (orange line, $p = 1.00$) and recovered (blue line, $b = 0.82$) aftershock rates.

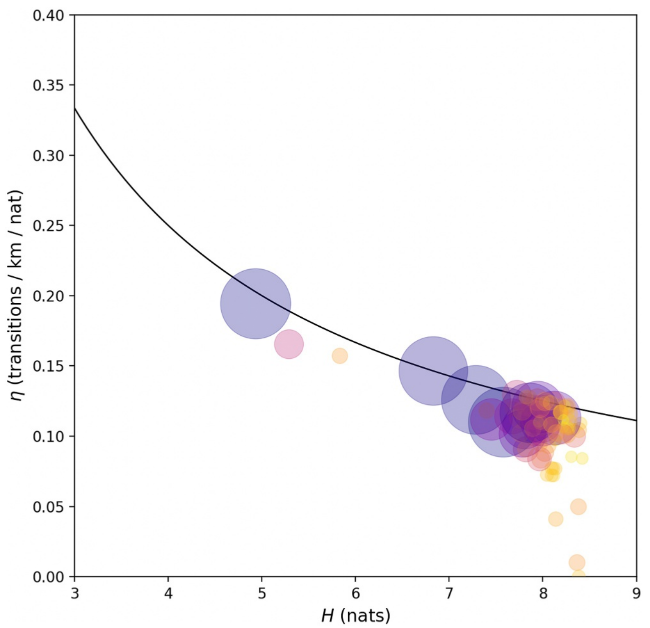

Figure 12. Entropy-normalized event location transition density, η, as a function of conditional entropy H. Each circle represents one event from the ensemble simulations, with symbol size proportional to magnitude (darker colors also indicate larger magnitudes). The black curve shows the theoretical model $\eta_{\max} \sim 1/H$. Events with lower entropy, $H \approx 5$–7 nats, exhibit higher sensitivity to loading perturbations $\eta \approx 0.2$, while high-entropy events, $H \approx 7.72$–8.25 nats, show reduced sensitivity, $\eta \approx 0.1$. Larger magnitude events exhibit some tendency to cluster at lower entropies due to their prescribed higher spatial selectivity exponent γ, which concentrates nucleation probability on fewer high geometric moment patches. Note that the event tracking algorithm is less certain for lower magnitude events.

approach. This latter approach encodes the assumption that over long periods of time, the rate of earthquakes can't go to zero nor increase unboundedly.

The statistical/kinematic/statical mechanics model developed here may serve both practical and philosophical purposes. It provides a means for generating long-duration earthquake catalogs, including finite-slip events over a wide range of magnitudes, at very low computational cost. This might enable the analysis of different sequence scenarios that are compatible with kinematic and statistical quantities that can be constrained by observations. Similarly, we have shown how this type of model can be used to develop sensitivities to both potentially measurable spatial loading variations and intrinsic randomness. Philosophically, a coarse-grained statistical earthquake sequence simulator is motivated by the observation that real fault systems exhibit consistent macroscopic behaviors (e.g., Gutenberg–Richter frequency distribution, Omori aftershock rate decay, magnitude-area scaling) that are better quantified than, and emerge from, the microscopic physics of friction, stresses, and fluid pressures that produce them. By coarse-graining at a level that doesn't depend on knowing details of fault properties and using the maximum entropy approach as a tool for developing an inference rule for spatial nucleation (and this might be extended in numerous ways), we model trade a continuum mechanics based understanding for quantitative statements about ensembles of plausible catalogs.

Upscaled fault slip representations based on continuum mechanics both frictional (Latour et al., 2011) and viscous (Pranger et al., 2022) have also emerged. In this context, it remains unclear whether there may be some type of conceptual convergence between upscaled mechanical models and kinematic and statistical mechanics type approaches developed here, or if more varied classes of earthquake sequence models will continue to be developed (for example, Burridge & Knopoff, 1967; Herz & Hopfield, 1995; Ismail-Zadeh et al., 2007; Richards-Dinger & Dieterich, 2012; Page & Field, 2026).

Algorithm 1: Earthquake sequence simulation algorithm.

```
Compute rate coefficient c (Equation 1)
for time steps do
  Release afterslip geometric moment form previous earthquakes (Equations 8 and 2)
  Increment tectonic loading (Equation 2)
  Determine earthquake rate (Equation 1)
  Accumulate rate to get number of events at time step, n
  if n > 0 then
      for each n do
          Compute spatial selectivity (Equations 4 and 6) and determine centroid
          location
          Draw event magnitude from Gutenberg-Richter distribution
          Generate coseismic slip distribution scaled to target magnitude
          Update released geometric moment and budget (Equation 2)
          Initialize afterslip sequence (Equation 8)
      end for
  end if
end for
```

Conflict of Interest

The author declares no conflicts of interest relevant to this study.

Availability Statement

All software developed for this project is available at (Meade, 2026). No data sources were used in this work.

Acknowledgments
No funding sources were involved in this work. We thank the editors and two thoughtful reviewers.

References

Allen, T. I., & Hayes, G. P. (2017). Alternative rupture-scaling relationships for subduction interface and other offshore environments. *Bulletin of the Seismological Society of America*, *107*(3), 1240–1253. https://doi.org/10.1785/0120160255

Asayesh, B. M., Hainzl, S., & Zöller, G. (2025). Improved aftershock forecasts using mainshock information in the framework of the ETAS model. *Journal of Geophysical Research*, *130*(2), e2024JB030287. https://doi.org/10.1029/2024jb030287

Barbot, S., Fialko, Y., & Bock, Y. (2009). Postseismic deformation due to the Mw 6.0 2004 parkfield earthquake: Stress-driven creep on a fault with spatially variable rate-and-state friction parameters. *Journal of Geophysical Research*, *114*(B7).

Båth, M. (1965). Lateral inhomogeneities of the upper mantle. *Tectonophysics*, *2*(6), 483–514. https://doi.org/10.1016/0040-1951(65)90003-X

Ben-Zion, Y. (2001). On quantification of the earthquake source. *Seismological Research Letters*, *72*(2), 151–152. https://doi.org/10.1785/gssrl.72.2.151

Ben-Zion, Y. (2008). Collective behavior of earthquakes and faults: Continuum-discrete transitions, progressive evolutionary changes, and different dynamic regimes. *Reviews of Geophysics*, *46*(4). https://doi.org/10.1029/2008rg000260

Berrill, J., & Davis, R. (1980). Maximum entropy and the magnitude distribution. *Bulletin of the Seismological Society of America*, *70*(5), 1823–1831.

Biemiller, J., Gabriel, A.-A., & Ulrich, T. (2023). Dueling dynamics of low-angle normal fault rupture with splay faulting and off-fault damage. *Nature Communications*, *14*(1), 2352. https://doi.org/10.1038/s41467-023-37063-1

Bilham, R., & Ambraseys, N. (2005). Apparent himalayan slip deficit from the summation of seismic moments for himalayan earthquakes, 1500–2000. *Current Science*, 1658–1663.

Borovkov, K., & Bebbington, M. (2003). A stochastic two-node stress transfer model reproducing omori's law. *Pure and Applied Geophysics*, *160*(8), 1429–1445. https://doi.org/10.1007/s00024-003-2354-8

Burridge, R., & Knopoff, L. (1967). Model and theoretical seismicity. *Bulletin of the Seismological Society of America*, *57*(3), 341–371. https://doi.org/10.1785/bssa0570030341

Carnot, S. (1824). Reflections on the motive power of fire, and on machines fitted to develop that power. *Bachelier*, *108*, 1824. https://www.asme.org/getmedia/e29ff2e8-c1b0-419b-8a15-7648a258aa65/carnot-brochure-final-2021.pdf

Churchill, R., Werner, M., Biggs, J., & Fagereng, Å. (2022). Afterslip moment scaling and variability from a global compilation of estimates. *Journal of Geophysical Research*, *127*(4), e2021JB023897. https://doi.org/10.1029/2021jb023897

Dascher-Cousineau, K., Shchur, O., Brodsky, E. E., & Günnemann, S. (2023). Using deep learning for flexible and scalable earthquake forecasting. *Geophysical Research Letters*, *50*(17), e2023GL103. https://doi.org/10.1029/2023gl103909

Dunham, E. M. (2007). Conditions governing the occurrence of supershear ruptures under slip-weakening friction. *Journal of Geophysical Research*, *112*(B7). https://doi.org/10.1029/2006jb004717

Erickson, B. A., Jiang, J., Barall, M., Lapusta, N., Dunham, E. M., Harris, R., et al. (2020). The community code verification exercise for simulating sequences of earthquakes and aseismic slip (SEAS). *Seismological Research Letters*, *91*(2A), 874–890. https://doi.org/10.1785/0220190248

Erickson, B. A., Jiang, J., Lambert, V., Barbot, S. D., Abdelmeguid, M., Almquist, M., et al. (2023). Incorporating full elastodynamic effects and dipping fault geometries in community code verification exercises for simulations of earthquake sequences and aseismic slip (SEAS). *Bulletin of the Seismological Society of America*, *113*(2), 499–523. https://doi.org/10.1785/0120220066

Fan, J., Zhang, F., Jiang, H., Xu, H., Cai, M., Cui, K., et al. (2025). A 25,000-yr-long integrated large earthquake record of the xiaojiang fault zone, southeastern Tibetan Plateau: New paleoseismic evidence from yangzong Lake. *Science China Earth Sciences*, *69*(2), 1–19. https://doi.org/10.1007/s11430-025-1772-1

Field, E. H., Milner, K. R., Hardebeck, J. L., Page, M. T., van der Elst, N., Jordan, T. H., et al. (2017). A spatiotemporal clustering model for the third uniform california earthquake rupture forecast (UCERF3-ETAS): Toward an operational earthquake forecast. *Bulletin of the Seismological Society of America*, *107*(3), 1049–1081. https://doi.org/10.1785/0120160173

Filippov, A., & Popov, V. (2010). Modified burridge–knopoff model with state dependent friction. *Tribology International*, *43*(8), 1392–1399. https://doi.org/10.1016/j.triboint.2010.01.010

Gutenberg, B., & Richter, C. F. (1944). Frequency of earthquakes in California. *Bulletin of the Seismological Society of America*, *34*(4), 185–188. https://doi.org/10.1785/BSSA0340040185

Herz, A. V., & Hopfield, J. J. (1995). Earthquake cycles and neural reverberations: Collective oscillations in systems with pulse-coupled threshold elements. *Physical Review Letters*, *75*(6), 1222–1225. https://doi.org/10.1103/physrevlett.75.1222

Ismail-Zadeh, A., Le Mouël, J.-L., Soloviev, A., Tapponnier, P., & Vorovieva, I. (2007). Numerical modeling of crustal block-and-fault dynamics, earthquakes and slip rates in the tibet-himalayan region. *Earth and Planetary Science Letters*, *258*(3–4), 465–485. https://doi.org/10.1016/j.epsl.2007.04.006

Ismail-Zadeh, A., & Soloviev, A. (2022). Numerical modelling of lithospheric block-and-fault dynamics: What did we learn about large earthquake occurrences and their frequency? *Surveys in Geophysics*, *43*(2), 503–528. https://doi.org/10.1007/s10712-021-09686-w

Jackson, D. D. (1996). Hypothesis testing and earthquake prediction. *Proceedings of the National Academy of Sciences*, *93*(9), 3772–3775. https://doi.org/10.1073/pnas.93.9.3772

Jaynes, E. T. (1957a). Information theory and statistical mechanics II. *Physical Review*, *108*(2), 171–190. https://doi.org/10.1103/PhysRev.108.171

Jaynes, E. T. (1957b). Information theory and statistical mechanics. *Physical Review*, *106*(4), 620–630. https://doi.org/10.1103/physrev.106.620

Johnson, K. M., Burgmann, R., & Larson, K. (2006). Frictional properties on the san andreas fault near parkfield, California, inferred from models of afterslip following the 2004 earthquake. *Bulletin of the Seismological Society of America*, *96*(4B), S321–S338.

Johnson, K. M., Fukuda, J., & Segall, P. (2012). Challenging the rate-state asperity model: Afterslip following the 2011 M9 tohoku-Oki, Japan, earthquake. *Geophysical Research Letters*, *39*(20). https://doi.org/10.1029/2012gl052901

Kaneko, Y., Avouac, J.-P., & Lapusta, N. (2010). Towards inferring earthquake patterns from geodetic observations of interseismic coupling. *Nature Geoscience*, *3*(5), 363–369. https://doi.org/10.1038/ngeo843

Kozdon, J. E., & Dunham, E. M. (2013). Rupture to the trench: Dynamic rupture simulations of the 11 march 2011 tohoku earthquake. *Bulletin of the Seismological Society of America*, *103*(2B), 1275–1289. https://doi.org/10.1785/0120120136

Lambert, V., Lapusta, N., & Faulkner, D. (2021). Scale dependence of earthquake rupture prestress in models with enhanced weakening: Implications for event statistics and inferences of fault stress. *Journal of Geophysical Research*, *126*(10), e2021JB021. https://doi.org/10.1029/2021jb021886

Lapusta, N., & Rice, J. R. (2003). Nucleation and early seismic propagation of small and large events in a crustal earthquake model. *Journal of Geophysical Research*, *108*(B4). https://doi.org/10.1029/2001jb000793

Lapusta, N., Rice, J. R., Ben-Zion, Y., & Zheng, G. (2000). Elastodynamic analysis for slow tectonic loading with spontaneous rupture episodes on faults with rate and state-dependent friction. *Journal of Geophysical Research*, *105*(B10), 23765–23789. https://doi.org/10.1029/2000jb900250

Latour, S., Campillo, M., Voisin, C., Ionescu, I., Schmedes, J., & Lavallée, D. (2011). Effective friction law for small-scale fault heterogeneity in 3D dynamic rupture. *Journal of Geophysical Research*, *116*(B10), B10306. https://doi.org/10.1029/2010jb008118

LeVeque, R. J., Waagan, K., González, F. I., Rim, D., & Lin, G. (2016). Generating random earthquake events for probabilistic tsunami hazard assessment. *Pure and Applied Geophysics*, *173*(12), 3671–3692. https://doi.org/10.1007/s00024-016-1357-1

Liu, D., Duan, B., Scharer, K., & Yule, D. (2022). Observation-constrained multicycle dynamic models of the southern san andreas and the northern san jacinto faults: Addressing complexity in paleoearthquake extent and recurrence with realistic 2D fault geometry. *Journal of Geophysical Research*, *127*(2), e2021JB023420. https://doi.org/10.1029/2021jb023420

Liu, Y., & Rice, J. R. (2005). Aseismic slip transients emerge spontaneously in three-dimensional rate and state modeling of subduction earthquake sequences. *Journal of Geophysical Research*, *110*(B8). https://doi.org/10.1029/2004jb003424

Lu, Y., Wetzler, N., Waldmann, N., Agnon, A., Biasi, G. P., & Marco, S. (2020). A 220,000-year-long continuous large earthquake record on a slow-slipping plate boundary. *Science Advances*, *6*(48), eaba4170. https://doi.org/10.1126/sciadv.aba4170

Mai, P. M., & Beroza, G. C. (2002). A spatial random field model to characterize complexity in earthquake slip. *Journal of Geophysical Research*, *107*(B11). https://doi.org/10.1029/2001JB000588

Main, I., & Naylor, M. (2012). Extreme events and predictability of catastrophic failure in composite materials and in the Earth. *The European Physical Journal Special Topics*, *205*(1), 183–197. https://doi.org/10.1140/epjst/e2012-01570-x

Main, I. G., & Naylor, M. (2008). Maximum entropy production and earthquake dynamics. *Geophysical Research Letters*, *35*(19). https://doi.org/10.1029/2008gl035590

Martyushev, L. M., & Seleznev, V. D. (2006). Maximum entropy production principle in physics, chemistry and biology. *Physics Reports*, *426*(1), 1–45. https://doi.org/10.1016/j.physrep.2005.12.001

Meade, B. (2026). Brendanjmeade/kes_paper: Paper_check_point [Software]. https://doi.org/10.5281/zenodo.18250115

Meade, B. J. (2024). A kinematic method for generating earthquake sequences. *Computers & Geosciences*, *184*(105), 105517. https://doi.org/10.1016/j.cageo.2023.105517

Neely, J. S., Salditch, L., Spencer, B. D., & Stein, S. (2023). A more realistic earthquake probability model using long-term fault memory. *Bulletin of the Seismological Society of America*, *113*(2), 843–855. https://doi.org/10.1785/0120220083

Ogata, Y. (1988). Statistical models for earthquake occurrences and residual analysis for point processes. *Journal of the American Statistical Association*, *83*(401), 9–27. https://doi.org/10.1080/01621459.1988.10478560

Ogata, Y., & Zhuang, J. (2006). Space–Time ETAS models and an improved extension. *Tectonophysics*, *413*(1–2), 13–23. https://doi.org/10.1016/j.tecto.2005.10.016

Oryan, B., & Gabriel, A.-A. (2025). Do coupled megathrusts rupture? *EarthArXiv Preprint*. https://doi.org/10.31223/X5HB3N

Page, M., & Field, E. (2026). An entropic explanation for gutenberg-richter scaling. *Journal of Geophysical Research: Solid Earth*, *131*(1), e2025JB032719. https://doi.org/10.1029/2025jb032719

Pranger, C., Sanan, P., May, D. A., Le Pourhiet, L., & Gabriel, A.-A. (2022). Rate and state friction as a spatially regularized transient viscous flow law. *Journal of Geophysical Research*, *127*(6), e2021JB023511. https://doi.org/10.1029/2021jb023511

Prigogine, I. (1978). Time, structure, and fluctuations. *Science*, *201*(4358), 777–785. https://doi.org/10.1126/science.201.4358.777

Reasenberg, P. A., & Jones, L. M. (1989). Earthquake hazard after a mainshock in California. *Science*, *243*(4895), 1173–1176. https://doi.org/10.1126/science.243.4895.1173

Rice, J. R., Lapusta, N., & Ranjith, K. (2001). Rate and state dependent friction and the stability of sliding between elastically deformable solids. *Journal of the Mechanics and Physics of Solids*, *49*(9), 1865–1898. https://doi.org/10.1016/s0022-5096(01)00042-4

Rice, J. R., & Tse, S. T. (1986). Dynamic motion of a single degree of freedom system following a rate and state dependent friction law. *Journal of Geophysical Research*, *91*(B1), 521–530.

Richards-Dinger, K., & Dieterich, J. H. (2012). RSQSim earthquake simulator. *Seismological Research Letters*, *83*(6), 983–990. https://doi.org/10.1785/0220120105

Ross, Z. E., Trugman, D. T., Hauksson, E., & Shearer, P. M. (2019). Searching for hidden earthquakes in southern California. *Science*, *364*(6442), 767–771. https://doi.org/10.1126/science.aaw6888

Rubin, A. M. (2008). Episodic slow slip events and rate-and-state friction. *Journal of Geophysical Research*, *113*(B11). https://doi.org/10.1029/2008jb005642

Rundle, P., Rundle, J., Tiampo, K., Donnellan, A., & Turcotte, D. (2006). Virtual California: Fault model, frictional parameters, applications. In *Computational earthquake physics: Simulations, analysis and infrastructure, part I* (pp. 1819–1846). Springer.

Salditch, L., Stein, S., Neely, J., Spencer, B. D., Brooks, E. M., Agnon, A., & Liu, M. (2020). Earthquake supercycles and long-term fault memory. *Tectonophysics*, *774*(228), 228289. https://doi.org/10.1016/j.tecto.2019.228289

Savage, J., & Langbein, J. (2008). Postearthquake relaxation after the 2004 M6 parkfield, California, earthquake and rate-and-state friction. *Journal of Geophysical Research*, *113*(B10). https://doi.org/10.1029/2008jb005723

Shaw, B. E. (1995). Frictional weakening and slip complexity in earthquake faults. *Journal of Geophysical Research*, *100*(B9), 18239–18251. https://doi.org/10.1029/95jb01306

Terada, T. (1933). On a measure of uncertainty regarding the prediction of earthquake based on statistics. *Proceedings of the Imperial Academy*, *9*(6), 255–257. https://doi.org/10.2183/pjab1912.9.255

Thurner, S., Hanel, R., & Klimek, P. (2018). *Introduction to the theory of complex systems*. Oxford University Press.

Thurston, R. H. (Ed.) (1897). *Reflections on the motive power of heat*. John Wiley and Sons.

Vallianatos, F., Papadakis, G., & Michas, G. (2016). Generalized statistical mechanics approaches to earthquakes and tectonics. *Proceedings of the Royal Society A: Mathematical, Physical and Engineering Sciences*, *472*(2196), 20160497. https://doi.org/10.1098/rspa.2016.0497

Venegas-Aravena, P., & Zaccagnino, D. (2025). Large earthquakes are more predictable than smaller ones. *Seismica*, *4*(1). https://doi.org/10.26443/seismica.v4i1.1568

Wei, M., Kaneko, Y., Liu, Y., & McGuire, J. J. (2013). Episodic fault creep events in California controlled by shallow frictional heterogeneity. *Nature Geoscience*, *6*(7), 566–570. https://doi.org/10.1038/ngeo1835

Weldon, R., Fumal, T., Powers, T., Pezzopane, S., Scharer, K., & Hamilton, J. C. (2002). Structure and earthquake offsets on the san andreas fault at the wrightwood, California, paleoseismic site. *Bulletin of the Seismological Society of America*, *92*(7), 2704–2725.

Yano, T. E., Takeda, T., Matsubara, M., & Shiomi, K. (2017). Japan unified high-resolution relocated catalog for earthquakes (JUICE): Crustal seismicity beneath the Japanese islands. *Tectonophysics*, *702*, 19–28. https://doi.org/10.1016/j.tecto.2017.02.017

Zhang, Y., Zhan, C., Huang, Q., & Sornette, D. (2024). Seismically informed reference models enhance AI-based earthquake prediction systems. *Journal of Geophysical Research*, *129*(3), e2023JB028037. https://doi.org/10.1029/2023jb028037